Optics Letters

Wavelength-scanning lensfree on-chip microscopy for wide-field pixel-super-resolved quantitative phase imaging

Xuejuan Wu,[1,2] Jiasong Sun,[1,2,3] Jialin Zhang,[1,2] Linpeng Lu,[1,2] Rong Chen,[1,2] Qian Chen,[2,4] and Chao Zuo[1,2,*]

[1]Smart Computational Imaging Laboratory (SCILab), School of Electronic and Optical Engineering, Nanjing University of Science and Technology, Nanjing, Jiangsu Province 210094, China
[2]Jiangsu Key Laboratory of Spectral Imaging & Intelligent Sense, Nanjing University of Science and Technology, Nanjing, Jiangsu Province 210094, China
[3]e-mail: sunjiasong@njust.edu.cn
[4]e-mail: chenqian@njust.edu.cn
*Corresponding author: zuochao@njust.edu.cn

Received 4 February 2021; revised 20 March 2021; accepted 21 March 2021; posted 22 March 2021 (Doc. ID 421869); published 19 April 2021

We propose a lensfree on-chip microscopy approach for wide-field quantitative phase imaging (QPI) based on wavelength scanning. Unlike previous methods, we found that a relatively large-range wavelength diversity not only provides information to overcome spatial aliasing of the image sensor but also creates sufficient diffraction variations that can be used to achieve motion-free, pixel-super-resolved phase recovery. Based on an iterative phase retrieval and pixel-super-resolution technique, the proposed wavelength-scanning approach uses only eight undersampled holograms to achieve a half-pitch lateral resolution of 691 nm across a large field-of-view of 29.85 mm^2, surpassing 2.41 times the theoretical Nyquist–Shannon sampling resolution limit imposed by the pixel size of the sensor (1.67 μm). We confirmed the effectiveness of this technique in QPI and resolution enhancement by measuring the benchmark quantitative phase microscopy target. We also showed that this method can track HeLa cell growth within an incubator, revealing cellular morphologies and subcellular dynamics of a large cell population over an extended period of time.

https://doi.org/10.1364/OL.421869

High-resolution wide-field microscopic imaging is playing an increasingly important role in many biomedical applications, including cell biology, digital pathology, and high-throughput drug screening [1]. Conventional microscopes are limited by the inherent tradeoff between objective magnification and field-of-view (FOV), making it difficult to achieve high-resolution and large FOV simultaneously. Although the introduction of mechanical scanning and image stitching can partially overcome this limitation by acquiring multiple images, it makes microscopy with large FOV complex and ill-suited for large-scale dynamic sample observations.

The emergence and rapid development of lensfree on-chip microscopy (LFOCM) in recent years have provided a promising solution to the above problems [2–5]. Object images are obtained across a wide FOV (native FOV of the image sensor) using a cost-effective and compact system without any lens. However, without geometric magnification (approximately 1×), the imaging resolution of LFOCM is limited by the sensor pixel size (typically >1 μm). To overcome this limitation, many pixel-super-resolution (PSR) methods have been proposed to reduce the effective pixel size through computational approaches, including sub-pixel shifting of illumination sources [6], sub-pixel lateral translation of image sensors [7], active parallel plate scanning [8], axial scanning with sample-to-sensor distances [9], etc.

In contrast to the above-mentioned PSR techniques, changing the illumination wavelength is a common practice in LFOCM to avoid complicated and time-consuming mechanical operations. In general, wavelength modulation techniques can be classified into two typical implementations: (1) individual multi-wavelength illuminations, e.g., red–green–blue (RGB) illuminations [10,11], where wavelength modulation is used as an alternative to the multi-height phase retrieval method based on the exchangeability of the illumination wavelength and propagation distance in the Fresnel diffraction formula. (2) Sequential wavelength scanning within a narrow spectral range (e.g., 10–30 nm) [12], where wavelength modulation is used as an alternative to the lateral shift-based PSR method.

As mentioned above, although the two categories of wavelength modulation techniques can solve the two major problems in LFOCM, i.e., phase recovery and PSR, independently, neither can achieve both high-resolution and high-quality quantitative phase imaging (QPI) without twin-image artifacts. For example, wavelength scanning in a narrow spectrum cannot produce sufficient diffraction diversity and transfer function coverage to achieve high-accuracy phase recovery

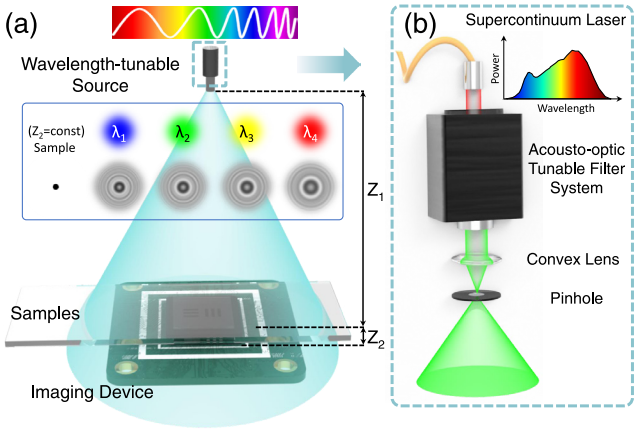

Fig. 1. Optical setup. (a) Schematic diagram of the proposed wavelength-scanning LFOCM. (b) Components of the wavelength-tunable source.

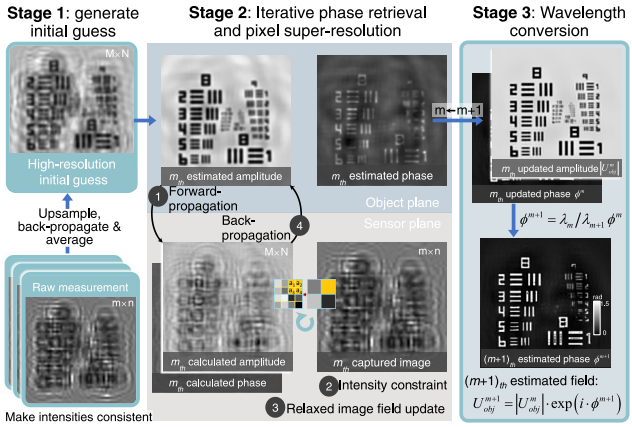

Fig. 2. Flowchart of the reconstruction algorithm for the proposed wavelength-scanning PSR.

[5,13,14]. Consequently, axial propagation, or illumination angle scanning, remains an essential procedure for creating sufficient diffraction effects [12]. However, this results in a significant increase in the amount of data acquisition (often requiring tens or even hundreds of raw measurements), precluding the long-term observation of dynamic samples. For this reason, high-resolution, long-term dynamic QPI of unlabelled biological samples based on an LFOCM has not yet been reported.

In this Letter, we propose a wavelength-scanning LFOCM approach for wide-field, pixel-super-resolved QPI. Our method achieves the complementary advantages of the two previous wavelength modulation methods by using a relatively large-range wavelength diversity, creating sufficient diffraction variations for both phase retrieval and resolution enhancement. Figure 1 depicts the configuration of our wavelength-scanning LFOCM system. In Fig. 1(b), the wavelength-tunable source is a supercontinuum laser (YSL SC-Pro) filtered by an acousto-optical tunable filter (AOTF, YSL AOTF-Pro bandwidths 2–9 nm). The wavelength λ can be adjusted from 430 nm to 1450 nm with a 1 nm interval. The coherent light from the source is spatially filtered by a 100 μm pinhole, creating a quasi-monochromatic spherical wavefront for sample illumination. After propagating ∼150 mm (Z_1), the wavefront is partially diffracted by the sample and generates in-line holograms to be recorded by a board-level monochrome CMOS sensor with a pixel size of 1.67 μm (3872 × 2764, The Imaging Source DMK 24UJ003), which is placed ∼0.5 mm (Z_2) below the sample plane.

In our system, the source-to-sample distance (Z_1) is large enough so that the illumination wavefronts can be approximated as plane waves. The illumination wavelength is tuned according to an incremental sequence $\{\lambda_m, m = 1, 2, 3, \ldots, M\}$ (M is the number of wavelengths), and the image sensor records a low-resolution hologram I^m_{cap} at wavelength λ_m. Figure 2 illustrates the overview flowchart of our reconstruction method, which is divided into three main stages:

Stage 1: Initialization. The raw images are first normalized with respect to their respective average intensity to compensate the nonuniformity of the power spectrum distribution of the supercontinuum laser, producing a normalized hologram sequence with consistent intensity $\{I^m\}$. All of the normalized holograms are bilinearly upsampled (the upsampling ratio is set to four in this Letter), then back-propagated to the object plane with the angular spectrum method, and finally averaged to generate an initial guess of the high-resolution object field corresponding to the first wavelength U^1_{obj}.

Stage 2: Iterative phase retrieval and PSR. This is the key step of the reconstruction algorithm, which can be further divided into four sub-steps.

(1) Forward propagation. The estimated object field U^m_{obj} corresponding to the m_{th} wavelength is forward-propagated to the image plane to obtain the image field U^m_{imag}.

(2) Intensity constraint. The intensity of the image field ($I^m_{\text{imag}} = |U^m_{\text{imag}}|^2$) is updated based on the intensity constraint imposed by the captured low-resolution hologram: $I^m_{\text{update}} = \frac{I^m_{\text{up}}}{I^m_{\text{imag\_bin}}} \times I^m_{\text{imag}}$, where I^m_{up} is a bilinearly upsampled version of I^m. $I^m_{\text{imag\_bin}}$ is calculated from I^m_{imag} by first pixel binning and then upsampling with the nearest neighborhood interpolation. This step guarantees that the updated intensity I^m_{update} after pixel binning coincides with the captured low-resolution intensity I^m.

(3) Relaxed image field update. The image field is updated in a recursive manner [9]: $U^m_{\text{update}} = (1-\alpha) \times U^m_{\text{imag}} + \alpha \times \sqrt{I^m_{\text{update}}} \cdot \exp[i \cdot \arg(U^m_{\text{imag}})]$, where $\arg(\cdot)$ is the function to obtain the argument, and α is the relaxation parameter controlling the amount of feedback from the previous estimate. Using a small step size of less than one (typically set to $1/M$) allows the intensity information of different wavelengths to blend together to reinforce the true signal while reducing the influence of noise.

(4) Back propagation. U^m_{imag} is back-propagated to the object plane to get the updated object field U^m_{obj} under λ_m.

Stage 3: Wavelength conversion. The object field U^m_{obj} should be converted to U^{m+1}_{obj} corresponding to the next wavelength. The absorption of the sample is assumed to be independent of the illumination wavelength, which is a reasonable assumption for most weakly scattering biology samples. The phase component should be changed proportionally ($\phi^{m+1} = \frac{\lambda_m}{\lambda_{m+1}}\phi^m$) while changing the wavelength. Moreover,

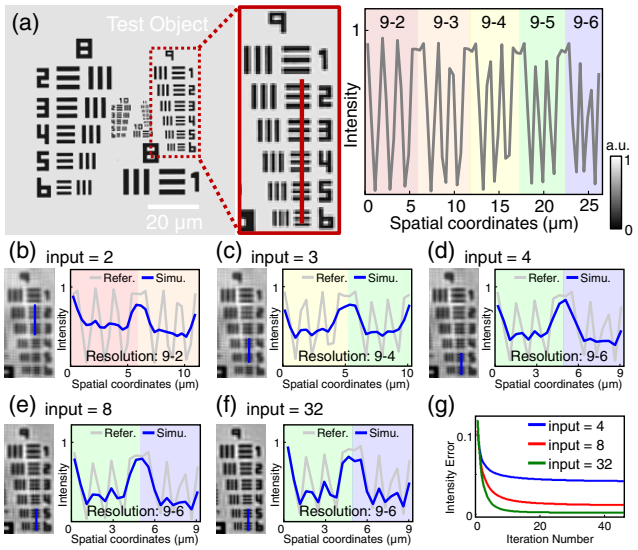

Fig. 3. Effect of the number of wavelengths on the reconstruction results. (a) High-resolution image of the simulated target. (b)–(f) Reconstructions (left) of five different numbers of wavelengths and the cross sections along the blue lines in the retrieved results (right). (h) Intensity mean absolute error versus iteration numbers.

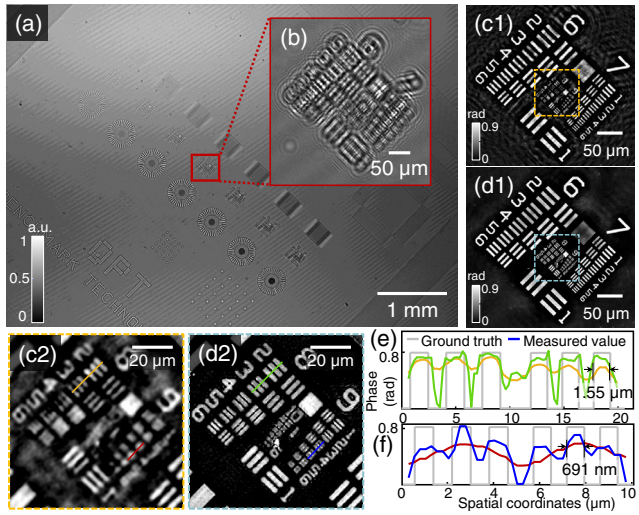

Fig. 4. Experimental results of QPT^{TM}. (a) Full-FOV raw hologram. (b) Enlarged region corresponding to the red boxed area in (a). (c1) Reconstruction from conventional multi-wavelength phase retrieval. (d1) Super-resolution reconstruction using our wavelength-scanning method. (c2) and (d2) Enlargement corresponding to the boxed areas in (c1) and (d1). (e)–(f) Phase values along the yellow, green, red, and blue lines in (c2) and (d2).

the wavelength conversion should be implemented on the unwrapped phase map, and additional two-dimensional phase unwrapping should be performed [15]. After wavelength conversion, the updated complex amplitude for the next sub-iteration is denoted as $U_{\text{obj}}^{m+1} = |U_{\text{obj}}^{m}|\exp(i \cdot \phi^{m+1})$.

Stages 2 and 3 are then repeated M times until all wavelengths have been used (all raw holograms have been processed once), which completes one iteration of the algorithm. The whole reconstruction process typically requires 5–20 iterations to converge (depending on the sample complexity and data quality), and the resultant U_{obj}^{m} provides the high-resolution amplitude and phase distribution of the measured object at wavelength λ_m.

To determine the required number of wavelengths, numerical simulations were carried out with parameters that fully reproduce our experimental system (pixel size 1.67 μm, sample-to-sensor distance 500 μm, wavelength-scanning range 450–520 nm). A 1951 USAF resolution target was used to quantify the resolution improvement, and the Group 9 features are extracted for better clarity [Fig. 3(a)]. The reconstructions corresponding to different numbers of wavelengths (2, 3, 4, 8, 32) are shown in Figs. 3(b)–3(f), respectively. It can be seen that eight wavelengths are sufficient to produce a high-quality reconstruction with Group 9 Element 6 clearly resolved, corresponding to a half-pitch resolution of 548 nm. Further increasing the number of wavelengths does not significantly improve the imaging resolution, but allows for faster convergence and lower steady-state errors [Fig. 3(g)]. Considering the tradeoff between acquisition efficiency and imaging resolution (such an imaging resolution is sufficient to reveal subcellular structures of live cells), we adopt eight wavelengths covering 450–520 nm with a 10 nm step for the subsequent experiments.

To verify the resolution enhancement of the proposed approach for QPI, we imaged a benchmark quantitative phase microscopy target (QPT^{TM}). Figure 4(a) shows one full FOV (~29.85 mm^2) low-resolution hologram captured at the 450 nm wavelength. The inset [Fig. 4(b)] shows an enlarged boxed area in Fig. 4(a) containing one typical group of resolution elements. Figures 4(c1)–4(c2) show the reconstructed phase distribution by using conventional multi-wavelength phase retrieval approaches without PSR [10], suggesting that only a half-pitch resolution close to the image sensor's pixel pitch [Group 8 Element 3, 1.55 μm, in Fig. 4(e)] can be achieved. In contrast, as shown in Figs. 4(d1)–4(d2), with our wavelength-scanning method, the half-pitch resolution can be enhanced to 691 nm [Group 9 Element 4, in Fig. 4(f)], surpassing 2.41 times the theoretical Nyquist–Shannon sampling resolution limit imposed by the pixel size of the sensor (1.67 μm). The slight gap between the experimentally achieved resolution (691 nm) and the simulation result (548 nm) may be attributed to instability of the light source, sensor noise, vibrations, and other experimental imperfections.

Finally, we demonstrate the wide-field pixel-super-resolved QPI capability of the proposed approach by long-term time-lapse imaging of live cells in culture. HeLa cells were seeded in a 35 mm glass-bottom Petri dish in Dulbecco's Modified Eagle's Medium supplemented with 10% fetal bovine serum. Thanks to the compactness of our system, it fits easily inside a cell culture incubator for *in situ* cell monitoring. A self-developed circuit was used as a programmable power switch for the camera to prevent overheating of the sensor surface (which might damage the cells inside the dish). It also generated control signal sequences to synchronize the camera with the AOTF. Without any physical moving components, our approach only used eight raw holograms at different illumination wavelengths (data acquisition took about 2 s) to recover a high-resolution wide-FOV quantitative phase image, permitting the study of the dynamic subcellular process with a high temporal resolution. In addition, the low light exposure and the absence of the fluorescent agents eliminate any concerns about phototoxicity and photobleaching, allowing for long-term (over 15 h) observation of cell growth in culture.

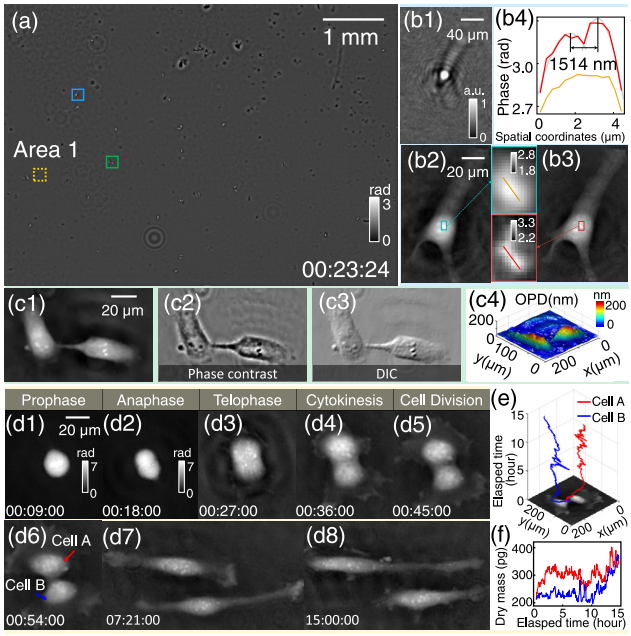

Fig. 5. Dynamic phase imaging of HeLa cells in culture (Visualization 1). (a) Phase reconstruction of the full FOV. (b1) Enlarged raw hologram; (b2) reconstruction by conventional multi-wavelength phase retrieval approach, and the zoom-in region corresponding to the dark cyan boxed area; (b3) super-resolution reconstruction using wavelength scanning, and the zoom-in region corresponding to the brown boxed area; (b4) phase values along the orange [in (b2)] and red [in (b3)] lines. (c1) Super-resolution reconstruction of the cell in the green box; (c2) simulated phase-contrast image; (c3) simulated DIC image; (c4) 3D rendering. (d1)–(d8) Eight selected time-lapse phase images of Area 1. (e) Dynamic tracking of the cells in Area 1. (f) Dry mass changes of two cells over time.

In Visualization 1, we provide the time-lapse movie of recovered full-FOV QPI with several zoom-in regions revealing details about subcellular dynamics. Figure 5(a) demonstrates one full-FOV reconstruction in this video, with two representative sub-regions (blue and green boxes) containing two individual cells magnified in Figs. 5(b3) and 5(c1). Once again, an improvement in resolution and SNR can be observed by comparing the reconstruction results of the conventional multi-wavelength phase retrieval approach [10] [Fig. 5(b2)] and the proposed wavelength-scanning approach [Fig. 5(b3)]. The red line profile in Fig. 5(b4) demonstrates a valley between two closely spaced features with a center-to-center distance of ~1.5 μm, and there is no such detailed feature in Fig. 5(b2). Based on the quantitative phase information retrieved, the phase contrast image, differential interference contrast (DIC) image, and pseudo-three-dimensional (3D) morphology (an accumulation of refractive index over the cell thickness) can be obtained computationally without resorting to additional hardware, as shown in Figs. 5(c2)–5(c4). In Figs. 5(d1)–5(d8), we further selected one cell [corresponding to the dashed-boxed region in Fig. 5(a)] to study its morphology during the whole observation process. Moreover, Figs. 5(d1)–5(d6) show the process of HeLa cell division, which spanned over 30 min. The high-resolution phase images clearly reveal the cell morphology at different phases of mitosis, including rounding up [Fig. 5(d1)], chromatin aggregation [Fig. 5(d2)], cytoplasm division [Fig. 5(d3)], and individualization of daughter cells [Fig. 5(d4)]. It should be noted that the phase information also allows for tracking trajectories of the cell family [Fig. 5(e)] and quantitatively analyzing the changes of the dry mass for individual cells [Fig. 5(f)]. These experimental results demonstrate the capability of the proposed wavelength-scanning LFOCM method for label-free, high-resolution, high-throughput, fast, long-term QPI in a traditional cell culture environment.

In summary, we have demonstrated a wavelength-scanning LFOCM technique for wide-field QPI. Our method generates pixel-super-resolved complex field reconstructions from a series of undersampled in-line holograms captured at multiple wavelengths within a relatively wide spectral range (450–520 nm), permitting fast, motion-free, QPI of unstained live samples. Experimental results demonstrate an improvement of the resolution of a wide-field LFOCM by a factor of 2.41, achieving a half-pitch resolution of 691 nm with a 1.67 μm pixel-size sensor using only eight intensity measurements. Cell culture experiments indicate that the proposed method offers a high-resolution, non-invasive, and high-throughout tool for *in vitro* long-term cell observations.

Funding. National Natural Science Foundation of China (61905115); Youth Foundation of Jiangsu Province (BK20190445); National Defense Science and Technology Foundation of China (2019-JCJQ-JJ-381); Leading Technology of Jiangsu Basic Research Plan (BK20192003).

Disclosures. The authors declare no conflicts of interest.

REFERENCES

1. H. R. Maricq and E. C. Carwile LeRoy, Arthritis Rheumatism **16**, 619 (1973).
2. A. Ozcan and U. Demirci, Lab Chip **8**, 98 (2008).
3. G. Zheng, S. A. Lee, Y. Antebi, M. B. Elowitz, and C. Yang, Proc. Natl. Acad. Sci. USA **108**, 16889 (2011).
4. H. Zhang, Z. Bian, S. Jiang, J. Liu, P. Song, and G. Zheng, Opt. Lett. **44**, 1976 (2019).
5. J. Zhang, J. Sun, Q. Chen, and C. Zuo, IEEE Trans. Comput. Imaging **6**, 697 (2020).
6. W. Bishara, T.-W. Su, A. F. Coskun, and A. Ozcan, Opt. Express **18**, 11181 (2010).
7. Y. Wu, Y. Zhang, W. Luo, and A. Ozcan, Sci. Rep. **6**, 28601 (2016).
8. J. Zhang, Q. Chen, J. Li, J. Sun, and C. Zuo, Opt. Lett. **43**, 3714 (2018).
9. J. Zhang, J. Sun, Q. Chen, J. Li, and C. Zuo, Sci. Rep. **7**, 11777 (2017).
10. P. Bao, F. Zhang, G. Pedrini, and W. Osten, Opt. Lett. **33**, 309 (2008).
11. C. Zuo, J. Sun, J. Zhang, Y. Hu, and Q. Chen, Opt. Express **23**, 14314 (2015).
12. W. Luo, Y. Zhang, A. Feizi, Z. Göröcs, and A. Ozcan, Light Sci. Appl. **5**, e16060 (2016).
13. W. Luo, Y. Zhang, Z. Göröcs, A. Feizi, and A. Ozcan, Sci. Rep. **6**, 22738 (2016).
14. C. Zuo, J. Li, J. Sun, Y. Fan, J. Zhang, L. Lu, R. Zhang, B. Wang, L. Huang, and Q. Chen, Opt. Laser Eng. **135**, 106187 (2020).
15. M. A. Herráez, D. R. Burton, M. J. Lalor, and M. A. Gdeisat, Appl. Opt. **41**, 7437 (2002).